UNIVERSIDADE ESTADUAL PAULISTA
"JÚLIO DE MESQUITA FILHO"
Câmpus de São José do Rio Preto

Massilon Oliveira Luizon

Estruturas Ocas de TiO_2 para Fotodegradação de Azul de Metileno no Espectro de Luz Visível.

São José do Rio Preto
2020

Massilon Oliveira Luizon

Estruturas Ocas de TiO_2 para Fotodegradação de Azul de Metileno no Espectro de Luz Visível.

Dissertação apresentada como parte dos requisitos para obtenção do título de Mestre em Nome do Programa, junto ao Programa de Pós-Graduação em Nome do Programa, do Instituto de Biociências, Letras e Ciências Exatas da Universidade Estadual Paulista "Júlio de Mesquita Filho", Câmpus de São José do Rio Preto.

Orientador: Prof. Dr. Diogo Paschoalini Volanti
Coorientador: Drª. Gabriela Byzynski Soares

São José do Rio Preto
2020

Luizon, Massilon Oliveira
L953n Estruturas ocas de TiO_2 para fotodegradação de azul de metileno no espectro de luz visível. / Massilon Oliveira Luizon. -- São José do Rio Preto, 2020
33 f.

Dissertação (mestrado) - Universidade Estadual Paulista (Unesp), Instituto de Biociências Letras e Ciências Exatas, São José do Rio Preto
Orientador: Diogo Paschoalini Volanti
Coorientadora: Gabriela Byzynski Soares

1. Estruturas ocas. 2. Fotodegradação de corantes. 3. hard template. 4. método hidrotermal por microondas. I. Título.

Sistema de geração automática de fichas catalográficas da Unesp. Biblioteca do Instituto de Biociências Letras e Ciências Exatas, São José do Rio Preto. Dados fornecidos pelo autor(a).

Massilon Oliveira Luizon

Estruturas Ocas de TiO_2 para Fotodegradação de Azul de Metileno no Espectro de Luz Visível.

Dissertação apresentada como parte dos requisitos para obtenção do título de Mestre em Nome do Programa, junto ao Programa de Pós-Graduação em Nome do Programa, do Instituto de Biociências, Letras e Ciências Exatas da Universidade Estadual Paulista "Júlio de Mesquita Filho", Câmpus de São José do Rio Preto.

Comissão Examinadora

Prof. Dr. Diogo Paschoalini Volanti
UNESP – Câmpus de São José do Rio Preto
Orientador

Profª. Drª. Iêda Aparecida Pastre Fertonani
UNESP – Câmpus de São José do Rio Preto

Drª. Elaine Cristina Paris
UFSCar – Câmpus de São Carlos

São José do Rio Preto
20 de dezembro de 2019

AGRADECIMENTOS

Aos meus pais que foram grandes incluenciadores e apoiadores da minha formação acadêmica,

Ao meu orientador e coorientadora, por todos os conhecimentos e experiências passados, assim como a confiança e apoio incondicional para minha passagem e conclusão dessa experiência científica e título,

Ao Ibilce que como instituição foi a ponte que ligou esses mundos,

O presente trabalho também foi realizado com apoio do Laboratório Nacional de Nanotecnologia, com suas instalações de XPS – LNNano/CNPEM (proposal no. 20389), e ao LME/IQ/Unesp e Embrapa/São Carlos pelas instalações de MET e MEV respectivamente aos quais sou grato,

O trabalho contou com apoio do Conselho Nacional de Desenvovimento Científico e Tecnológico. - Brasil (CNPQ) - Código de Financiamento 444926/2014-3, à qual agradeço,

E também agradeço à FAPESP pelo apoio financeiro concedido ao laboratório, sob o processo nº 2013/23886-4, 2014/17343-0, 2015/04511-5, 2017/01267-1 - Fundação de Amparo à Pesquisa do Estado de São Paulo (FAPESP).

“Grandes espíritos sempre encontraram oposição de mentes medíocres. A mente medíocre é incapaz de entender o homem que se recusa a curvar- se cegamente aos preconceitos convencionais e escolhe ao invés disso expressar suas opiniões honestamente e com coragem.”

Albert Einstein (2011, p. 149)

RESUMO

A aceleração induzida das reações de superfície em fotocatalisador pela luz visível, é um fator crucial para melhorar a separação das reações redox e, assim, aumentar o desempenho do fotocatalisador. No entanto, a preparação de fotocatalisadores com uma estrutura bem definida e com uma alta área superficial continua sendo um desafio significativo. Neste trabalho, este artigo apresenta uma estratégia fácil e rápida para a síntese de flocos ocos de TiO_2 com controle de sua forma e tamanho de partículas, para fotodegradação do corante azul de metileno. Os flocos de TiO_2 foram preparados usando nanoflocos de α-Fe_2O_3 com a técnica de "*hard template*" para o crescimento de TiO_2 utilizando o método hidrotermal assistido por microondas. Nossos resultados confirmam que os flocos ocos de TiO_2 apresentam estruturas de anatase cristalina com alta área superficial. Além disso, a ligeira diminuição no intervalo de banda e o aumento da dispersão da luz pelas amostras ocas promovem o aumento da atividade fotocatalítica para a descoloração do azul de metileno. O mecanismo de fotocatálise sob luz do espectro visível foi proposto, indicando que os sítios reacionais no composto oco de TiO_2 promovem a transferência de carga com menor comprimento de onda da luz. A fotodegradação do azul de metileno pelos flocos ocos de TiO_2 está correlacionada à dispersão ou reflexão da luz por estruturas ocas, além da maior área superficial desse tipo de morfologia que suprime a recombinação elétron-buraco do fotocatalisador.

Palavras–chave: Estruturas ocas; Método hidrotermal por micro-ondas; Fotodegradação de corantes; Moldes duros.

ABSTRACT

The visible-light-induced acceleration of photocatalyst surface reactions is a crucial factor in improving the separation of redox reactions and thus increasing photocatalyst performance. However, preparing photocatalysts as a well-defined structure with a high surface area remains a significant challenge. Herein, this paper presents an easy and fast strategy for the synthesis of TiO_2 hollow flakes with particle shape and size control to methylene blue dye photodegradation. The TiO_2 flakes were prepared using α-Fe_2O_3 nanoflakes as hard-template for TiO_2 growth under the microwave-assisted hydrothermal method. Our results confirm that TiO_2 hollow flakes present crystalline anatase flakes structures with a high surface area. Also, the slight decrease in the bandgap and the increase in light scattering by hollow samples promotes the enhancement of photocatalytic activity for methylene blue discoloration. The photocatalytic mechanism under visible illumination was proposed, indicating that trapped sites in hollow TiO_2 flakes promote the charge transfer with lower light wavelength. The photodegradation of methylene blue by TiO_2 hollow flakes is correlated to the scattering or reflection of light by hollow structures, in addition to the larger surface area of this type of morphology that suppresses electron-hole recombination of the photocatalyst.

Keywords: Hollow structure; Microwave-assisted hydrothermal; Photodegradation of dyes; Hard template.

LISTA DE ILUSTRAÇÕES

LISTA DE TABELAS

LISTA DE ABREVIATURAS E SIGLAS

eV Elétron-Volts (unidade de medida).

UV Ultra Violeta.

@ Símbolo para definição de uma hétero estrutura.

ACS American Chemical Society (define grau de pureza de reagente).

GHz Giga-Heartz (unidade de medida).

W Watts (unidade de medida).

RPM Rotações por Minuto.

JCPDS Joint Committee on Powder Diffraction Standants (Database de dados - XRD).

SUMÁRIO

1. Introduction

The design morphology control synthesis of photocatalyst has attracted attention in recent years because of size/shape dependence of some materials properties as chemical, optical, magnetic, catalytic, and electrical for examples [2,3]. To improve some specific properties, as a photocatalytic activity, many kinds of structures could be obtained as hierarchical nanospheres [4], hollow spheres [5], flowers-like [6], nanotubes [7], nanocubes [8], nanosheets [9] and nanowires [10]. In the case of photocatalysis, morphology with large surface area allows an efficiency improve [11], such as hollow structures. The hollow and porous particles with uniform sizes become a potentially useful material's structure in different application areas, due to some properties as high specific surface area, low effective density, and good diffusion of external molecules [2]. Some properties like incident light scatter and reflection by hollow structures improve the photocatalytic process as the light intensity increases [12].

Recently, the use of hard templates to obtain hollow nanostructures is widespread [12–15] and enables to obtain hollow nanostructures with controllable shape and size, being the Fe_2O_3 material, one of the most used for this purpose [2,16,17]. Of all the semiconductors used in the photocatalytic process, TiO_2 is one of the most commonly used semiconductors, due to its wide bandgap energy (3.2 eV), which confines the photoactivity under the ultraviolet (UV) region [18]. TiO_2 hollow spheres structures show a significant photocatalytic performance with increasing absorption characteristics [19,20]. Song et al. proposed by the two-dimensional anatase TiO_2 hollow nanoflakes with the large specific surface area, suitable dye-photocatalyst contact areas, and more active sites for rhodamine-B photodegradation [5]. Authors suggested that significant photocatalytic performance of TiO_2 hollow nanoflakes is due to the anatase phase presence with smaller nanocrystals size and an increase in surface defects as the calcination temperature decrease.

Based on the previous discussion, in this work is presented the TiO_2 hollow structure obtained through the microwave-assisted hydrothermal method and the visible light photocatalysis application. The synthesis is based in α-Fe_2O_3 (hematite) hard-template uses, with TiO_2 interaction over all the template structure. The hard-template (α-Fe_2O_3), the heterostructure (α-Fe_2O_3@TiO_2) and the hollow sample (TiO_2 hollow) morphologies show similar structure, as nanoflakes morphology for α-Fe_2O_3 and α-Fe_2O_3@TiO_2 and hollow morphology for TiO_2 hollow sample. The crystalline phase shows pure hematite for α-Fe_2O_3, anatase phase for TiO_2 hollow and the hematite with anatase phase for α-Fe_2O_3@TiO_2. UV-vis

diffusive reflectance shows there is an increase in visible absorption wavelength for α-Fe_2O_3@TiO_2 and TiO_2 hollow. The methylene blue degradation under visible light confirms the photocatalytic active higher for TiO_2 hollow sample compared to the other samples.

2. Objectives

This paper aims to contribute in the understanding of the optical and electronical properties of hollow semiconductors structures, through the practical application in a photocatalysis of methylene blue as an indicator. On this matter, will be evaluate semiconductors isolated (α-Fe_2O_3 and TiO_2 hollow sample) also the heterostructures with both of these composites. For this, will be conduced a well-structured synthesis and also chemical characterization, morphological and electronic in the composites forming on synthesis. After that, will occur the evaluation of the photo degradation efficiency of these semiconductors.

3. Experimental section

3.1. Synthesis procedure

α-Fe_2O_3 flakes. The procedure was adapted from Song et al. work [5]. Then, 0.48g of aluminum sulfate hydrate (≥97%, Sigma-Aldrich) was added on 30 mL aqueous iron (III) nitrate nonahydrate (ACS reagent, ≥98%, Sigma-Aldrich) solution (0.2 mol L^{-1}) under magnetic stirring. Then, 30 mL of concentrated ammonium hydroxide solution (ACS reagent, 28.0-30.0% NH_3 basis, Sigma-Aldrich) was slowly dropped in the solution under magnetic stirring during 10 min. The previous solution transferred to a sealed polytetrafluorethylene reactor and heated at 160°C for 90 minutes in a microwave apparatus (2.45 GHz/800 W) [21]. The resulted powder was then washed with deionized water, centrifuged, and dried at 60°C overnight.

α-Fe_2O_3@TiO_2. The 100 mg of previous α-Fe_2O_3 flakes sample was sonicated with 200 mL of ethanol (ACS reagent, ≥99.5%, Sigma-Aldrich) for 90 minutes. Then, 1.8 mL of titanium (IV) butoxide (TB) (reagent grade, 97%, Aldrich) was added to the solution under magnetic stirring and, 0,5 mL of the concentrated ammonia solution (ACS reagent, 28.0-30.0% NH_3 basis, Sigma-Aldrich) was added. The resulted solution remained under magnetic stirring for 12 h. After that, the resulted precipitate was washed four times, alternatively, with deionized water and ethanol, and then centrifuged (7,500 rpm during 5 minutes). After the wash step, the sample was dried at 60°C overnight. The resulted compound was heat-treated in the muffle furnace at 350°C for 2 hours with a heat rate of 1°C min^{-1}.

TiO_2 hollow flakes. The obtained heterostructure on the last step was placed in a bottom flask with, 50mL solution (2 mol L^{-1}) of hydrochloric acid (37%, Chemis), and continuously homogenized, with a rotary evaporator (40 rpm) in a temperature bath at 100 °C for 9 hours. The water cooling was turned on, but the solvent was not evaporated much staying the most of it on the flask, during all procedure. After the 9 hours' time, the solution color turns from dark orange to a pale yellow, an indication of the α-Fe_2O_3 extraction into ions Fe^{3+} in the solvent, also is observed a white precipitate identified as TiO_2, confirming that the α-Fe_2O_3 template was effectively removed. The hollow structure was then collected after washing with water and ethanol, dried after the last wash at 60°C overnight. This sample was labeled as TiO_2 hollow flakes. The centrifuge stats for every step of synthesis was 7500 rpm for 5 minutes each washing liquid.

3.2. Characterizations

The X-ray powder diffraction (XRD) patterns obtained with Higaku MiniFlex 300 diffractometer (Cu K_α radiation (λ = 1.5418 Å)), scanning from 2θ of 20° to 80°, at 2° min^{-1}, were used to obtain the samples phase composition and crystalline structure. N_2 physisorption (Micromeritics Germini VII) was used to obtain the surface areas (SA) of the synthesized samples, using the Brunauer- Emmett-Teller (BET) method. Diffuse reflectance UV–vis spectra were obtained using an ultraviolet-visible–near-infrared (UV–vis–NIR) Cary 5G spectrophotometer. Powder morphology and size was characterized by field emission scanning electron microscopy (FE-SEM) with JEOL Microscope - Model JSM 6701F. Transmission electron microscopy (TEM) (and high-resolution HRTEM) images, selected area electron diffraction (SAED) patterns, and energy dispersive X-ray spectra (EDS) were obtained using a Philips model CM200 instrument operated at an accelerating voltage of 200 kV. X-ray photoelectron spectroscopy (XPS) (Thermo K-alpha XPS Thermo Scientific, Inc.) were used to evaluate the chemical composition of samples with radiation of Al K_α, under vacuum condition and 400 μm spot size. The Survey spectral resolution was 1 eV with ten scans, and higher resolution spectra were 0.1 eV with 50 scans.

3.3. Photocatalytic degradation activity

Photocatalytic studies were carried out for the discoloration of methylene blue (MB) (2.5 mg L^{-1}) dye solution. 2mg of each powder sample was dissolved in 20 mL of MB solution, in separate beakers, under magnetic stirring. The solutions were then illuminated with six visible light sources (Philips lamps, 15W, and maximum intensity at 440 nm), during two hours,

with magnetic stirring at a constant temperature of 25 ºC, and aliquots were taken at intervals of 30 minutes. A UV–vis spectrophotometer (Shimadzu-UV- 1601 PC spectrophotometer) was used to monitor modifications in optical absorption of the resultant solutions throughout the experiment. A control sample, without catalysts, was also performed (photolysis). MB photo-discoloration was conducted on the average of triplicate experiments.

4. Results and discussion

It is well known that the morphology is related to materials performance and the use of template allows a controlled nanoparticles growth, and, different architected structures are possible to obtain. In this way, the α-Fe_2O_3 material was chosen due to the earth abundance, low cost, nontoxicity, and reasonably design. The aluminum sulfate solution controls the α-Fe_2O_3 morphology as described by FE-SEM results. At the time that titanium (IV) butoxide reagent was dispersed in α-Fe_2O_3 alcoholic solution, the resulted dispersion modifies the color from dark orange to light orange, resulting in a precipitate. The color modification is an indication that the titanium precursor effectively interacts with α-Fe_2O_3 particles. The following procedure, the α-Fe_2O_3 extraction, the color of the solution also changed, from light orange to pale yellow, and a white precipitate was observed, indicating that the process was effective. During the synthesis methods, it was obtained three different samples: α-Fe_2O_3, α-Fe_2O_3@TiO_2, and TiO_2 hollow. X-ray diffraction analysis (XRD) was used to obtain the crystalline phase of synthesized samples (Figure 1). The phase composition of α-Fe_2O_3 sample is identified as pure hematite phase (JCPDS 33-664), indicating the high crystallinity of template material. For the TiO_2 hollow sample, XRD results confirm the pure TiO_2 anatase phase (JCPDS 21-1272), showing that the template extraction process does not affect the crystallinity nor the purity of the TiO_2 hollow sample. Song et al.[5] show the high purity and crystallinity of the TiO_2 hollow nanoflakes obtained with 48 hours synthesis process route. Even though the intermediated sample before the template extraction process, the α-Fe_2O_3@TiO_2, presents a mixture of phase composition. By XRD analysis, the α-Fe_2O_3@TiO_2 sample is composed by α-Fe_2O_3 hematite phase (JCPDS 33-664) and TiO_2 anatase phase (JCPDS 21-1272), indicating that the template presence does not affect the TiO_2 anatase phase growth.

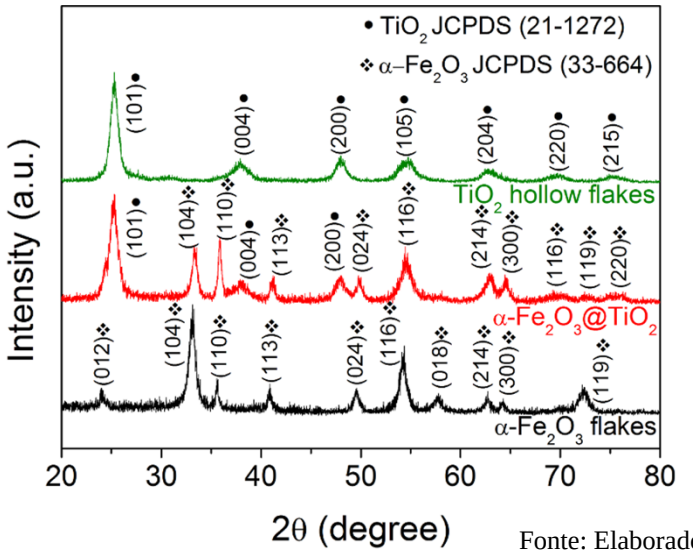

Fonte: Elaborado pelo autor.

Figure 1. XRD analysis of α-Fe_2O_3 flakes, α-Fe_2O_3@TiO_2, and TiO_2 hollow flakes.

Figure 2 shows the FESEM images of α-Fe_2O_3 flakes (Figure 2a), α-Fe_2O_3@TiO_2 (Figure 2b), and TiO_2 hollow (Figure 2c) samples. The α-Fe_2O_3 presents morphology homogeneity with nanoflakes shape, which is a crucial characteristic to considerate as a hard template material. It is also observed a very few nanoflakes material with some fractures. The morphology of α-Fe_2O_3 is induced by aluminum sulfate salt during the synthesis process, modifying the growth particles mechanism compared with previously reported in the literature [3,22,23]. The nanoflakes α-Fe_2O_3 size are average 550 nm; with some smaller nanoflakes (~350 nm) diameter, and the nanoflakes thickness is average 5 nm. The addition of titanium (IV) butoxide (TB) solution in hard template material does not modify the resulted morphology of nanoflakes, showing similar nanoflakes morphology for the α-Fe_2O_3@TiO_2 sample. From Figure 2b, the surface charged of hard template α-Fe_2O_3 is adequate to promote a good loaded of TiO_2 particles. Nanoflakes α-Fe_2O_3@TiO_2 size is average 650 nm and the thickness increases (~95 nm) compared with the hard template material, endorsing that the TB addition process as the synthesis of the α-Fe_2O_3@TiO_2 sample was effective. Figure 2b shows the α-Fe_2O_3@TiO_2 sample surface composed of many small TiO_2 nanoparticles. The TiO_2 hollow sample (Figure 2c) shows similar morphology structure as the α-Fe_2O_3@TiO_2 sample, demonstrating nanoflakes morphology with a thickness of ~ 95 nm and the average size of 700 nm. The hard-template extraction process does not affect the morphology of the resulted material. However, the FESEM image clearly shows some fractures and breaks in nanoflakes caused eventually by the hard-template extraction process.

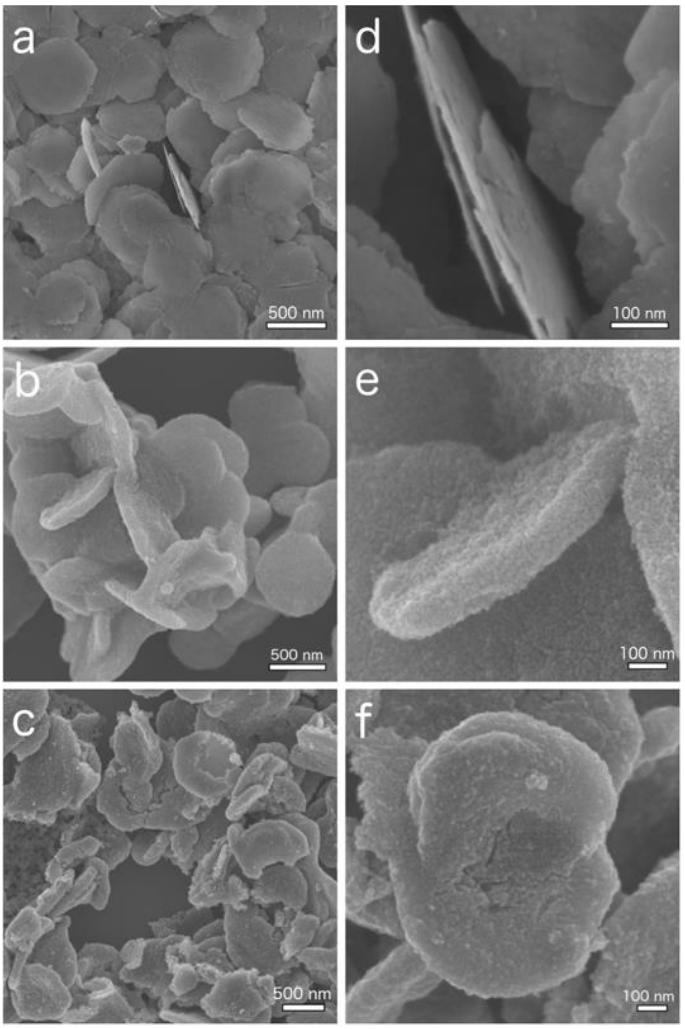

Fonte: Elaborado pelo autor.

Figure 2. FESEM images of (a) α-Fe_2O_3 flakes, (b) α-Fe_2O_3@TiO_2, and (c) TiO_2 hollow flakes. The respective details of each particle are in the images on the right (d), (e), and (f), respectively.

The size and morphology results were confirmed through the TEM imagens of corresponding obtained samples synthesized by microwave hydrothermal method, Figure 3. From the TEM observation, it can be confirmed the spherical morphology homogeneity with nanoflakes shape of α-Fe_2O_3 (Figure 3a), α-Fe_2O_3@TiO_2 (Figure 3d) samples and, the most important, the hard template extraction process does not modify the morphology of TiO_2 hollow samples (Figure 3g). HRTEM analyses were used to confirm the crystallinity of the samples. Figure 3b presents the HRTEM image of α-Fe_2O_3 sample where it is possible to confirm the presence of (110) planes of α-Fe_2O_3 hematite phase (JCPDS 33-664). Also, the same crystalline phase is confirmed through SAD results (Figure 3C) with the (110) and (300) planes of α-Fe_2O_3 hematite phase. The HRTEM and SAD images of the α-Fe_2O_3@TiO_2 sample (Figure 3e and f) confirm the presence of α-Fe_2O_3 hematite phase, observed through (012) plane in HRTEM image and (113) and (024) planes in the SAD image. Also, the TiO_2 anatase phase (JCPDS 21-

1272) was present in the α-Fe_2O_3@TiO_2 sample, confirmed through the (101) plane in HRTEM image and (101) and (004) planes in the SAD image. For TiO_2 hollow sample, HRTEM and SAD images (Figure 3h and i) confirm the presence of TiO_2 anatase phase due to the (101) plane observed in HRTEM image and (101), (103), and (200) planes observed in the SAD image (JCPDS 21-1272). Any crystalline iron impurity was observed in HRTEM, and SAD results of TiO_2 hollow samples confirmed the efficiency of the hard-template extraction process.

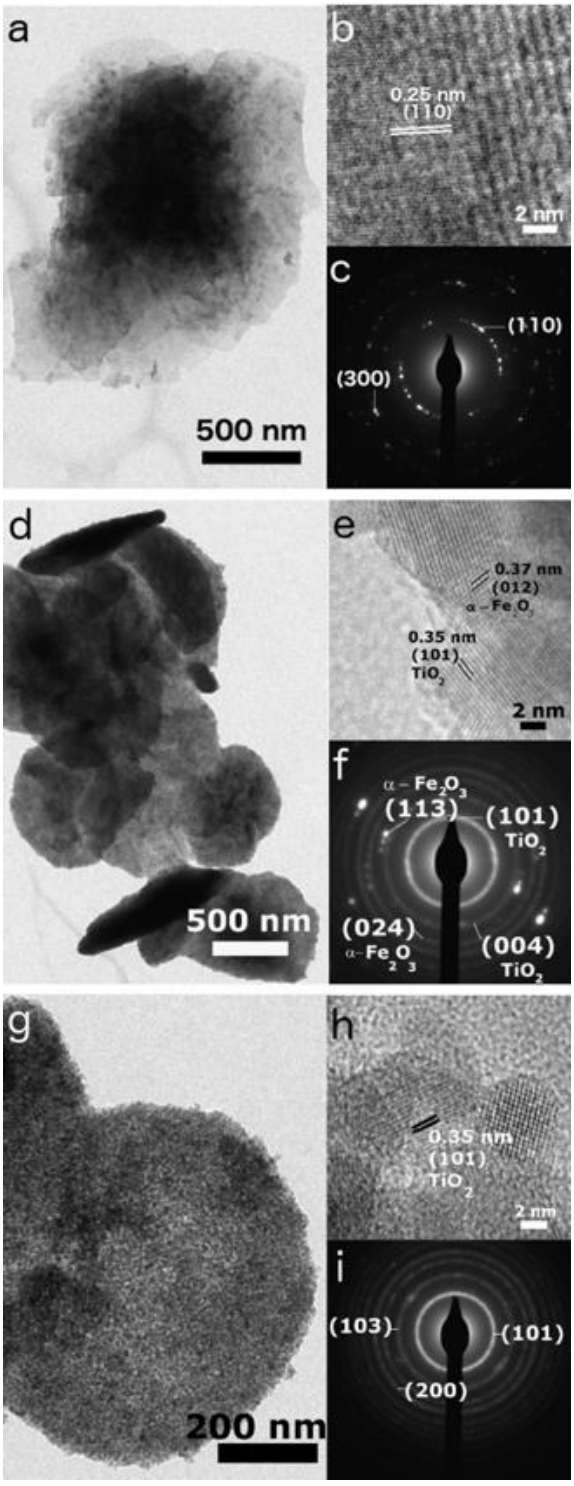

Fonte: Elaborado pelo autor.

Figure 3. TEM image of (a) α-Fe_2O_3 flakes, HRTEM of (b) α-Fe_2O_3 flakes, and SAED of (c) α-Fe_2O_3 flakes. Image of TEM of (d) α-Fe_2O_3@TiO_2, HRTEM of (e) α-Fe_2O_3@TiO_2, and SAED of (f) α-Fe_2O_3@TiO_2. Image of TEM of (g) TiO_2 hollow flakes, HRTEM of (h) TiO_2 hollow flakes, and SAED of (i) TiO_2 hollow flakes.

EDS analysis was employed to independently determine the different chemical element presence, as shown in Figure 4. The presence of Cu in all samples is related to the sample holder or glass substrate. Furthermore, EDS results show that Fe and Al are observed in α-Fe_2O_3 and α-Fe_2O_3@TiO_2 samples. The presence of Al is related to aluminum sulfate salt used during the synthesis process to control the α-Fe_2O_3 morphology. Neither Fe nor Al was observed in TiO_2 hollow samples, indicating the efficiency of the hard-template extraction process. EDS result of TiO_2 hollow shows the presence of Ti, as in EDS results of the α-Fe_2O_3@TiO_2 sample.

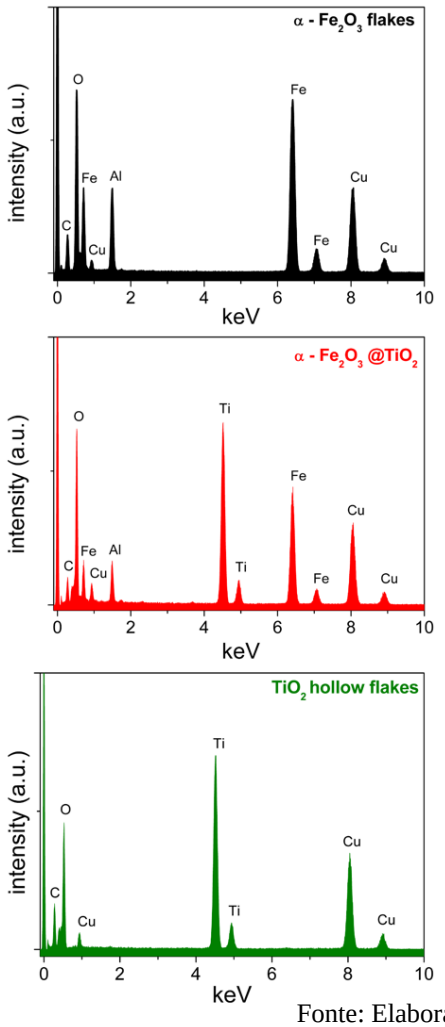

Fonte: Elaborado pelo autor.

Figure 4. EDS spectra of α-Fe_2O_3 flakes, α-Fe_2O_3@TiO_2, and TiO_2 hollow flakes.

So far, from the electron microscopic images, it is observed that several nanostructures of α-Fe_2O_3 hematite compose the nanoflakes structures presented by FE-SEM images. Based on the mechanism proposed by Chakrabarty and Chatterjee [3], spherical units of $Fe(OH)_3$/Fe(O)(OH) nuclei is assumed to initiate the formation of α-Fe_2O_3, based in oriented attachment crystal growth mechanism. The orientation of nuclei is influenced by the solvent used in the synthesis process and by the presence of $Al_2(SO_4)_3$ in the synthesis medium, which could control the α-Fe_2O_3 nanoflakes shape. During the crystal growth of α-Fe_2O_3 nanoflakes, nucleation and aggregation events compete, controlling the diffusion rate of the solute due to solvent viscosity, affecting the $Fe(OH)_3$/Fe(O)(OH) nuclei formation. Although the oriented aggregation explains the nuclei formation, it is possible that Ostwald ripening process also occurs, describing the growth of larger crystals at the detriment of smaller ones, as FE-SEM and TEM images depict nanoflakes α-Fe_2O_3 size as average 550 nm. The crystal growth mechanism of Fe_2O_3@TiO_2 sample only differ from the α-Fe_2O_3 sample by the secondary particles layer of TiO_2 formed through aggregation of subunits of Ti^{4+} ions, in an oriented and irreversible way under α-Fe_2O_3 crystals, already formed. After the sintering process that Fe_2O_3@TiO_2 sample was submitted, anatase TiO_2 is formed. In this way, Fe_2O_3@TiO_2 crystal growth mechanism suffers more impact of a self-aggregation process than the Ostwald ripening process. For TiO_2 hollow structure, the crystal growth mechanism is the same as Fe_2O_3@TiO_2 sample, with an additional step, the hard-template (α-Fe_2O_3) extraction, which did not modify the morphology structure. Iron presents a strong bonding and low mobility on TiO_2 surface, promoting stabilization of four or fewer iron atoms [24]. The specific surface area (SSA) of each sample determined by N adsorption BET methods, corroborates with FESEM images. SSA results for α-Fe_2O_3, α-Fe_2O_3@TiO_2, and TiO_2 hollow samples are presented in Table 1. The hard-template sample presents the lowest SSA of all samples, as presented by FE-SEM images as thin nanoflakes morphologies. For the α-Fe_2O_3@TiO_2 sample, SSA increases with the addition of the TiO_2 nanoparticles. The hard-template extraction (TiO_2 hollow) allows that SSA increases, even more, indicating a hollow structure formation.

Table 1: Superficial surface area and bandgap energy of the α-Fe_2O_3 flakes, α-Fe_2O_3@TiO_2, and TiO_2 hollow flakes samples.

Samples	**Surface Area ($m^2.g^{-1}$)**	**Bandgap energy (eV)**
α-Fe_2O_3 flakes	73.64 ± 1.22	1.98
α-Fe_2O_3@TiO_2	118.24 ± 1.28	2.03
TiO_2 hollow flakes	136.85 ± 1.28	3.22

The UV-vis absorption spectra of α-Fe_2O_3, α-Fe_2O_3@TiO_2, and TiO_2 hollow samples confirmed the different absorption behavior of samples in Figure 5. The α-Fe_2O_3 sample exhibits a higher energy absorbance edge in the visible light region of 450 – 650 nm than α-Fe_2O_3@TiO_2, which shows more similar absorption behavior compared to α-Fe_2O_3 than to TiO_2 hollow. That behavior is consistent with the color of the sample. The strong absorption in the visible region of α-Fe_2O_3 and α-Fe_2O_3@TiO_2 samples indicate that these samples can be used in the process as photocatalysis under visible illumination. The TiO_2 hollow sample absorbed ultraviolet radiation (325 – 400 nm) and a slightly part of visible radiation (400 – 500 nm). The absorption behavior of the TiO_2 hollow samples is similar to commercial anatase TiO_2 exhibited by Li et al. [25], which shows only ultraviolet radiation absorption in less than 400 nm. Table 1 presents the bandgap of α-Fe_2O_3 and α-Fe_2O_3@TiO_2 samples considering a direct electronic transition. The $(\alpha h\upsilon)^2$ *vs.* hυ relation allowed the bandgap determination as depicted in the inset of Figure 5. The direct bandgap of α-Fe_2O_3 sample is 1.98 eV, which indicates the transition of O^{2-} 2p → Fe^{3+} 3d and is similar to presented by α-Fe_2O_3 nanocrystals obtained by the hydrothermal method [22]. The bandgap of the α-Fe_2O_3@TiO_2 sample (2.03 eV) presents a slight increase compared with α-Fe_2O_3 sample, revealing that TiO_2 over layers did not widely modify the absorption edge and is similar with band gaps of Fe_2O_3–TiO_2 photoanodes for solar water oxidation [26]. The α-Fe_2O_3 and α-Fe_2O_3@TiO_2 samples present possibilities with visible light irradiation use, as visible photocatalysis. Due to the more elevated band gap value of α-Fe_2O_3@TiO_2, it is possible to induce that the charge (electron-hole) recombination rate during photocatalytic events decreases compared with α-Fe_2O_3 sample. On the other hand, the TiO_2 hollow sample is considered as an indirect semiconductor, and the $(\alpha h\upsilon)^{1/2}$ *vs.* hυ relation present in an insert in Figure 5, showing a bandgap value of 3.22 eV. Is evident that the α-Fe_2O_3 extraction did not affect the crystallographic structure of anatase TiO_2, as presented in DRX results. Neither the characteristic absorption of anatase TiO_2 is affected by hard-template extraction since the bandgap value found by the TiO_2 hollow samples is comparable to the commercial Degussa P25 presented by some authors [27].

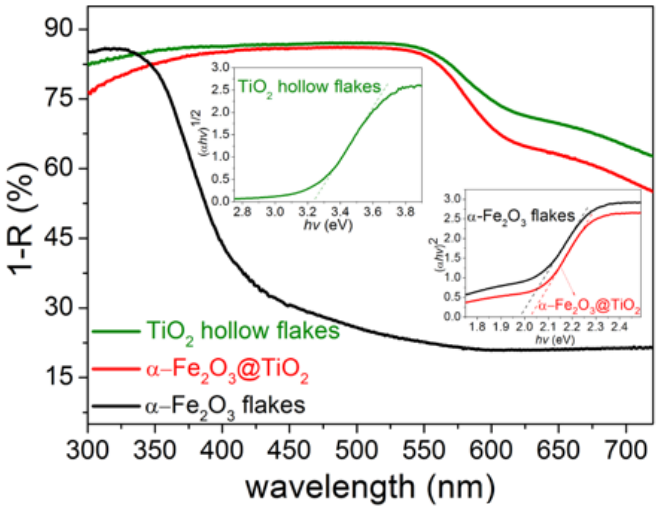

Fonte: Elaborado pelo autor.

Figure 5. UV-vis absorption spectra of α-Fe_2O_3 flakes, α-Fe_2O_3@TiO_2, and TiO_2 hollow flakes. Insets: relation of $(\alpha h\upsilon)^2$ *vs.* hυ for all samples.

The surface chemical compositions as the valence states of Fe, Ti, and O ions of samples were analyzed by X-ray photoelectron spectroscopy (XPS) (Figure 6 and Figure S1) to confirm the chemical composition of samples. The survey scanning spectrum (Figure S1) indicates the presence of C (Figure S2) for all samples. However, for the α-Fe_2O_3 sample, the survey scanning spectrum indicates the presence of Fe, C, and O and for the TiO_2 hollow sample, the presence of Ti, Fe, O and C elements. Table 2 presents the quantification obtained by XPS results of each element present in samples. The high-resolution O 1s spectra were deconvoluted into three components (Figure 6a), and for the α-Fe_2O_3 sample, the peak at 528.9 eV confirms the presence of O - Fe specific energy binding and the peak at 530.05 eV indicates hydroxyl ions, adsorbed over the surface sample. In the same Figure 6a, for the TiO_2 hollow sample, the peak at 529 eV is assigned to the metallic oxide Ti-O binding energy in the TiO_2 lattice, the peak 530.05 eV corresponds to hydroxyl ions and, 531 eV, to water molecule adsorbed over the surface sample. For the α-Fe_2O_3@TiO_2 sample, the high-resolution O 1s spectrum shows a peak at 529.06 eV, corresponding to O-Fe and Ti-O bonding. Hydroxyl ions adsorbed on the material surface is also observed at 530 eV binding energy, as adsorbed water at 531 eV binding energy [28]. The high-resolution Ti 2p spectra (Figure 6b) for the TiO_2 hollow sample is consistent with the peak values of Ti^{4+} in the TiO_2 lattice, with two spin-orbital peaks at 463.5 and 457.8 eV, corresponding to Ti $2p^{1/2}$ and Ti $2p^{3/2}$ spin-orbital splitting photoelectrons, respectively. Furthermore, for the α-Fe_2O_3@TiO_2 sample, Ti 2p spectrum shows similar peaks characteristics to TiO_2 confirming the presence of the Ti^{4+} ions over the material surface

constituted by the α-Fe_2O_3 hard-template sample, as previously reported in material and methods sections.

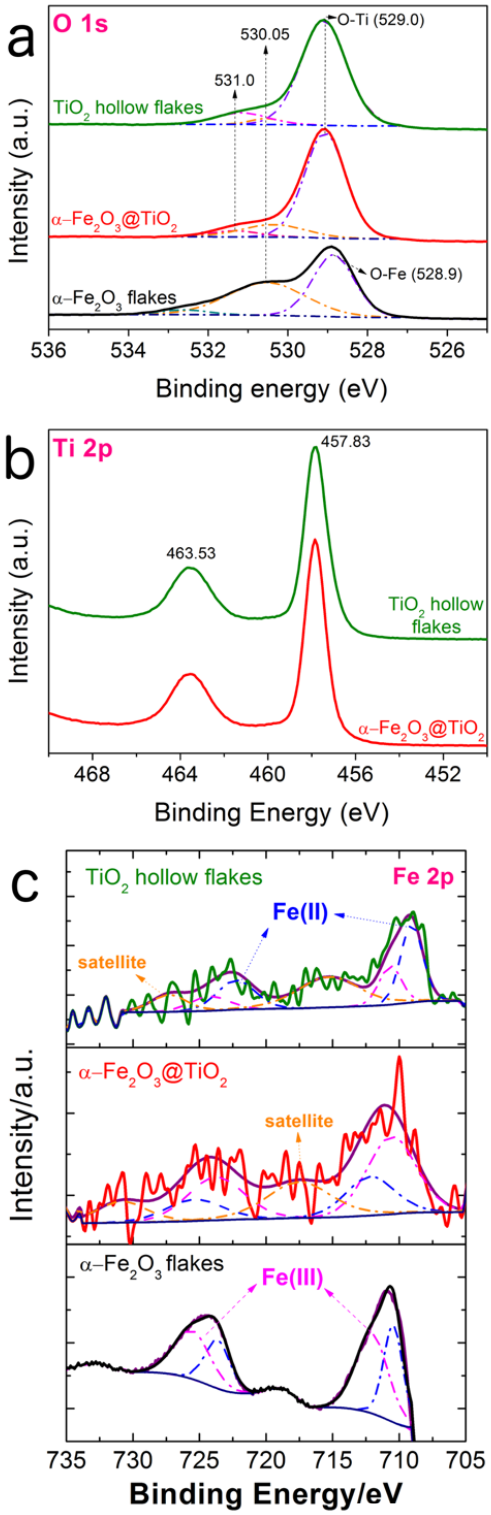

Fonte: Elaborado pelo autor.

Figure 6. O 1s high-resolution XPS spectra (a), Ti 2p high-resolution XPS spectra (b), and Fe 2p high-resolution XPS spectra for α-Fe_2O_3 flakes, α-Fe_2O_3@TiO_2, and TiO_2 hollow flakes.

In high-resolution Fe 2p spectra (Figure 6c) for α-Fe_2O_3, α-Fe_2O_3@TiO_2 and TiO_2 hollow samples present two distinct peaks at binding energies about 720 and 709 eV, corresponding to Fe $2p^{1/2}$ and Fe $2p^{3/2}$ spin-orbital splitting photoelectrons, respectively [29]. Each spin-orbital peak is deconvoluted in two more peaks, indicating the presence of Fe^{2+} (in lower binding energy values) and Fe^{3+} (in higher binding energy values). Another piece of evidence to the existence of both iron oxidation states is the satellite peaks indicated in Figure 6c. However, spectra intensities are not similar for all cited samples. For the α-Fe_2O_3 sample, Fe 2p spectrum intensity is higher than the other two samples, α-Fe_2O_3@TiO_2, and TiO_2 hollow. The material composition of the α-Fe_2O_3@TiO_2 sample promotes a decrease in Fe 2p spectrum intensity since the TiO_2 particle cover all the surface of α-Fe_2O_3 template material, as XPS analysis is a surface analysis. However, the Fe 2p spectrum of the TiO_2 hollow samples shows the two characteristics Fe 2p spin-orbital splitting photoelectrons, indicating that in the extraction process of the α-Fe_2O_3 hard-template, there is still left slightly small quantity of Fe ions. In this way, the Fe ions remnants could be used as seeds for TiO_2 lattice grow, modifying some material physical-chemical characteristics. For the quantification obtained through XPS results (Table 2), only Fe $2p^{3/2}$ spin-orbital peak was used, similar to titanium quantification, where only Ti $2p^{3/2}$ spin-orbital peak was considered. The valence state of Ti did not suffer any alteration; however, the valence state of Fe modify. Initially inserted in the reaction solution as Fe (III), sulfate ions present in the synthesis of α-Fe_2O_3 nanoflakes synthesis promote the reduction to Fe (II) following the equation 1 [30].

$$Fe^{3+} + 2\,SO_4^{2-} \rightarrow Fe^{2+} + S_2O_8^{2-} \quad (1)$$

As the three samples were obtained based in the same reaction, all the samples present a content of Fe^{2+} and Fe^{3+}, indicated in Table 2. After the initial reaction between iron (III) nitrate and aluminum sulfate, there are no sulfate ions remnants in the surface powders, which could influence further characterization. For α-Fe_2O_3@TiO_2 sample, the Fe quantification is just an illustration as the XPS analysis is energetically enough only to provide surface results and, in the case, the samples are covered through TiO_2 nanoparticles.

Table 2: XPS quantification results of α-Fe_2O_3 flakes, Fe_2O_3@TiO_2 and TiO_2 hollow flakes.

	α-Fe₂O₃ flakes		***α-Fe₂O₃@TiO₂***		***TiO₂ hollow flakes***	
	Position (eV)	**Content (%)**	**Position (eV)**	**Content (%)**	**Position (eV)**	**Content (%)**
C 1s	284.53	26.81 ± 3.00	284.80	23.35 ± 0.70	284.80	25.82 ± 3.74
	286.03	4.68 ± 0.12	286.83	1.44 ± 0.71	286.80	1.96 ± 0.34
	287.53	1.31 ± 0.47	287.33	2.11 ± 0.60	288.13	2.41 ± 0.78
	288.53	3.45 ± 0.21	288.78	1.98 ± 0.48	287.97	1.74 ± 0.30
O 1s	529.43	28.18 ± 2.03	529.88	42.55 ± 1.09	530.55	30.01 ± 19.57
	531.03	27.22 ± 2.98	531.59	9.18 ± 0.81	531.28	19.83 ± 21.24
	533.18	1.97 ± 0.51				
Ti 2p$^{3/2}$	-	-	460.55	19.11 ± 0.31	458.62	17.96 ± 1.67
Fe 2p$^{3/2}$	710.18	5.99 ± 1.10	710.32	0.15 ± 0.04	709.50	0.17 ± 0.02
	711.98	3.79 ± 0.58	712.34	0.11 ± 0.06	711.10	0.10 ± 0.03

Figure 7a shows the visible photocatalytic activity of Methylene blue (MB) discoloration with synthesized samples during 120 minutes. The kinetic rate (k´) for samples classified as a pseudo-first-order reaction [31], presented in Figure 7B, with R^2 for α-Fe_2O_3, α-Fe_2O_3@TiO_2 and TiO_2 hollow samples as 0.973, 0.993 and 0.997, respectively. The photocatalytic active semiconductor surface could be related to superficial area values, classifying the photocatalytic process as a surface-dependent process. In this way, the kinetic rate is normalized by a superficial area of each sample. Figure 7a and 7b confirm that with α-Fe_2O_3@TiO_2 and TiO_2 hollow samples, photo-generated charge carriers could be separated under visible illumination. The α-Fe_2O_3 sample does not present photocatalytic activity under visible illumination since its behavior is similar to MB photolysis. The bandgap value of α-Fe_2O_3 is the smallest one compared with another sample, indicating a possible charge recombination increase even through during visible illumination.

Holes/electrons photogeneration under visible light is an essential issue for diverse semiconductors materials to produce active, visible materials, used in water splitting process, solar cells performance, and photocatalysis process. Some methods are applicable such as employing the semiconductors heterostructures [23,25,28,32,33] or dope the semiconductor [18,34–37], to improve the light-harvesting, mainly in the visible region. The α-Fe_2O_3@TiO_2 sample is classified as a semiconductor heterostructure and presents singular photocatalytic

activity under visible illumination compared with the hard-template (α-Fe_2O_3), due to the charge carrier separation caused by heterostructure composition (heterostructure Type I). Furthermore, Fe cations act as trap centers for the photo-charge carriers (electrons/holes), enhancing the electrons/holes lifetime and, consequently, inducing a better separation between them and enhance the photocatalytic performance of the α-Fe_2O_3@TiO_2 sample [33]. In the case of α-Fe_2O_3 sample, the distance between trapping sites decreases, resulting in a more elevated rate of charge carrier recombination through quantum tunneling. The photocatalytic performance is then reduced due to the consummation of the charge carrier recombination in the redox reaction over the photocatalyst surface [33].

Liu et al. [38] present the Rhodamine-B photocatalytic activity of Fe_2O_3@TiO_2 under UV illumination obtained via sol-gel and affirm that OH* radical is the major radical involved in the photocatalytic activity and a redox center of Fe^{3+}/Fe^{2+} inhibits the charge carrier recombination. Li et al. [25] show the MB photocatalytic degradation of the α-Fe_2O_3@TiO_2 sample under visible illumination via co-precipitation method, which exhibits better photocatalytic performance than TiO_2 powder. Authors attribute the photocatalytic efficiency to higher absorption of heterostructure material in the visible light region. The number of α-Fe_2O_3 and TiO_2 interfacial layers is the principal responsible for increasing the absorption under visible light illumination[28]. In this way, the α-Fe_2O_3@TiO_2 sample presents k´ value higher than the α-Fe_2O_3 sample, as indicated in Figure 7b.

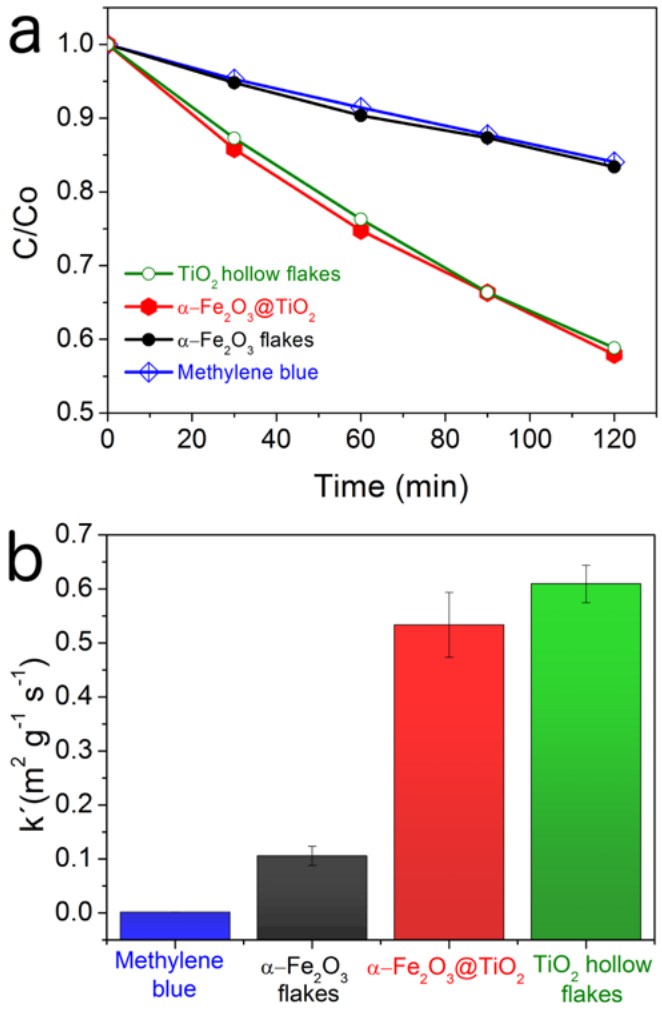

Fonte: Elaborado pelo autor.

Figure 7. (a) Kinetic results and, (b) kinetic rate (k´) of methylene blue degradation under visible illumination with α-Fe_2O_3 flakes, α-Fe_2O_3@TiO_2, and TiO_2 hollow flakes samples.

The SSA and the absorption under visible light illumination are more significant for the α-Fe_2O_3@TiO_2 sample than the α-Fe_2O_3 sample, as presented by DRS results, promoting an increase in photocatalytic activity under visible illumination. For the TiO_2 hollow samples, the MB degradation efficiency is similar to the α-Fe_2O_3@TiO_2 sample under visible illumination. During 120 minutes of irradiation, ~ 65% of initial MB concentration was degraded. Song et al. [5] exhibit an impressive Rhodamine-B photocatalytic activity of TiO_2 hollow nanoflakes obtained by a similar method proposed under UV illumination. Authors attributed the increase in photocatalytic to unique hollow and surface state, allowing more active sites to participate in the degradation reaction. In this way, become more easily dye molecules transport until the active sites and, promoting an enhancing in photocatalysis.

In the case of MB degradation (TiO_2 hollow sample), which show the highest k´ value for MB, the particular hollow structure and the highest superficial area (SSA) could facilitate

the degradation process. Furthermore, even the DRS results show a considerable band gap value, the visible photocatalytic performance of the TiO_2 hollow sample is expressive. In this way, the remnants Fe cations, confirmed in XPS results, play a significant role in the TiO_2 hollow structure as trap centers for photo-charge carriers, even more than in the α-Fe_2O_3@TiO_2 sample, reducing the photo-charge carrier recombination [36,39].

The α-Fe_2O_3@TiO_2 sample is classified as a conventional heterojunction photocatalysts type I, which the interface between α-Fe_2O_3 and TiO_2 particles result in a straddling gap of band alignment, i.e., the CB and VB of TiO_2 semiconductor are respectively higher and lower than the CB and VB of α-Fe_2O_3 semiconductor. The light incident can promote electrons from both VB to CB (TiO_2 and α-Fe_2O_3) to CB, creating a hole (positive charge – h^+) in the VB and electron (negative charge – e^-) in the CB. The charge carrier is conducted to lower energies bands, which is CB and VB of α-Fe_2O_3, resulting in a reduction/oxidation reaction involved in the photocatalytic process. The heterojunction photocatalysts Type I show an increase in charge carrier recombination, due to the bandgap resulted diminished compared with the bandgap of the separated semiconductor. However, due to the bandgap modification, the photocatalytic activity in the visible region is efficient. The photocatalytic mechanism for TiO_2 hollow sample is based on two factors: first one and the principal is the increase in light intensity absorbs during illumination process due to hollow structure and, the second factor, in the visible illumination, the dye sensitizing mechanism takes place. The incident light reflects on hollow material surface as normal particle morphology; however, there are transmitted lights and further reflections inside hollow structure, resulting in multi-reflection of incident light (A general and green approach to synthesize monodisperse ceria hollow spheres with enhanced photocatalytic activity, efficient hollow double-shell photocatalysts for the degradation of organic pollutants under visible light and in darkness).

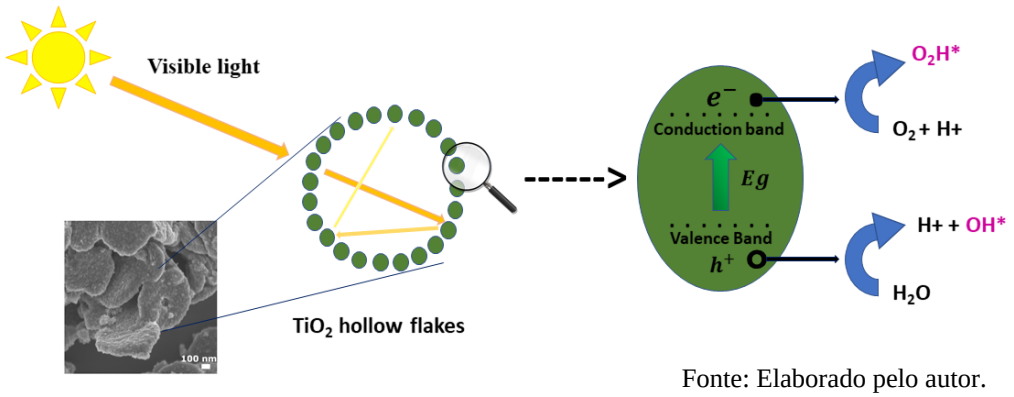

Fonte: Elaborado pelo autor.

Figure 8. Proposed mechanism for the photocatalytic activity of TiO_2 hollow samples.

The multi-reflection of incident light with the high density of active sites due to the increase in surface area of TiO_2 hollow material favors the photocatalytic activity efficiency. In this way, the photocatalytic process illustrated in Figure 8, started with TiO_2 hollow sample surface illumination with a specific wavelength ($h\upsilon$), creating the charge carrier hole/electron (h^+/e^-), equation 2.

$$TiO_2 + h\nu \rightarrow e_{CB}^- + h_{VB}^+ \quad (2)$$

In VB region, the photogenerated hole reacts with surface adsorbed water, producing hydroxyl radicals and cationic hydrogen, equation 3.

$$h_{VB}^+ + H_2O \rightarrow OH^* + H^+ \quad (3)$$

On the other hand, in CB region, photogenerated electrons react with molecular oxygen adsorbed in TiO_2 hollow surface, producing radical oxygen (O_2^-) (equation 6). Subsequently, O_2^- reacts with H^+ produced in equation 4, generating superoxide radical (O_2H^*).

$$e_{CB}^- + O_2 \rightarrow O_2^- + H^+ \rightarrow O_2H^* \quad (4)$$

Finally, oxygenated radical production attack MB molecules, promoting a discoloration in MB initial solution, until CO_2 and H_2O are produced equations 5 and 6. The intermediates of the MB degradation are not the scopus of the paper.

$$OH^* + MB \rightarrow H_2O + CO_2 \quad (5)$$
$$O_2H^* + MB \rightarrow H_2O + CO_2 \quad (6)$$

Another reaction that probably occurs with TiO_2 hollow sample in visible photocatalysis is the dye sensitizing mechanism. MB molecules absorb visible light and are excited (MB*); consequently, the MB* could transfer and electron to CB of TiO_2 hollow sample, promoting an increase in superoxide radical production. Therefore, the hollow structure enables the increase in light incident efficiency use due to the multi-reflection caused by hollow structure and consequently, increasing the photocatalytic activity. The TiO_2 hollow structure presents SSA higher than the other samples, indicating an increase in photocatalytic active sites in the hollow structure. In this way, trapped sites possible increase, promoting a charge transfer with lower wavelength illumination. As a result, the charge carriers recombination decreases, resulting in an enlargement on visible photocatalytic efficiency. Finally, the dye sensitizing mechanism take place and allow even more the visible photocatalytic activity of TiO_2 hollow sample.

5. Conclusion

TiO_2 hollow flakes was obtained by a fast, easy, and green method under microwave-assisted hydrothermal synthesis. TiO_2 nanoflakes hollow structures were synthesized by α-Fe_2O_3 nanoflakes structure after loading by TiO_2 nanoparticles. The hard-template extraction does not alter the main crystalline phase of TiO_2 anatase, however, improved the superficial surface area obtained through BET isotherms. Although the band gap value of TiO_2 hollow suffers slightly reduced compared to commercial TiO_2, the TiO_2 hollow exhibit an improvement in visible photocatalytic activity. The behavior is correlated with the increase in light scattering and transmittance of hollow particle favors the improvement in photocatalytic activity of methylene blue discoloration. The visible photocatalytic discoloration mechanism of methylene blue was discussed. The results promoted a better understanding of TiO_2 hollow structures in photocatalytic activity, enabling the use of the same element as a hard-template search.

Acknowledgments

The authors acknowledge the financial support from the São Paulo Research Foundation – FAPESP (grants 2013/23886-4, 2014/17343-0, 2015/04511-5, 2017/01267-1), and from the National Council for Scientific and Technological Development – CNPQ (grant 444926/2014-3). The Brazilian Nanotechnology National Laboratory provided the XPS facilities – LNNano/CNPEM (proposal no. 20389). TEM and FESEM analyses were provided by LME/IQ/Unesp and Embrapa/São Carlos, respectively.

References

[1] A. Calaprice, The ultimate quotable Einstein, 2011. doi:10.5860/choice.48-6340.

[2] J. Lian, X. Duan, J. Ma, P. Peng, T. Kim, W. Zheng, Hematite (α-Fe_2O_3) with Various Morphologies: Ionic Liquid-Assisted Synthesis, Formation Mechanism, and Properties, ACS Nano. 3 (2009) 3749–3761. doi:10.1021/nn900941e.

[3] S. Chakrabarty, K. Chatterjee, Oriented growth of α-Fe_2O_3 nanocrystals with different morphology and their optical behavior, J. Cryst. Growth. 381 (2013) 107–113. doi:10.1016/j.jcrysgro.2013.07.013.

[4] Y.L. Pang, S. Lim, H.C. Ong, W.T. Chong, Research progress on iron oxide-based magnetic materials: Synthesis techniques and photocatalytic applications, Ceram. Int. 42 (2016) 9–34. doi:10.1016/j.ceramint.2015.08.144.

[5] C. Song, L. Wang, F. Gao, Q. Lu, Two-Dimensional Hollow TiO_2 Nanoplates with

Enhanced Photocatalytic Activity, Chem. - A Eur. J. 22 (2016) 6368–6373. doi:10.1002/chem.201504570.

[6] H. Xu, Z. Wu, M. Ding, X. Gao, Microwave-assisted synthesis of flower-like BN/BiOCl composites for photocatalytic Cr(VI) reduction upon visible-light irradiation, Mater. Des. (2016). doi:10.1016/j.matdes.2016.10.057.

[7] A. Rónavári, D. Kovács, C. Vágvölgyi, Z. Kónya, M. Kiricsi, I. Pfeiffer, Ion exchange defines the biological activity of titanate nanotubes, J. Basic Microbiol. 56 (2016) 557–565. doi:10.1002/jobm.201500742.

[8] S.W. Verbruggen, TiO2 photocatalysis for the degradation of pollutants in gas phase: From morphological design to plasmonic enhancement, J. Photochem. Photobiol. C Photochem. Rev. 24 (2015) 64–82. doi:10.1016/j.jphotochemrev.2015.07.001.

[9] X. Wang, Y. Li, C. Wang, T. Gan, J. Yan, J. Wang, Ultrathin $Na_2Ti_9O_{19}$ heterostructural nanosheets modified with TiO_2 nanoparticles for enhanced photocatalysis, Mater. Lett. 178 (2016) 140–143. doi:10.1016/j.matlet.2016.04.206.

[10] H.F. Wilson, C. Tang, A.S. Barnard, Morphology of Zinc Oxide Nanoparticles and Nanowires: Role of Surface and Edge Energies, J. Phys. Chem. C. (2016) acs.jpcc.6b01479. doi:10.1021/acs.jpcc.6b01479.

[11] S.-Y. Pung, W.-P. Lee, A. Aziz, Kinetic Study of Organic Dye Degradation Using ZnO Particles with Different Morphologies as a Photocatalyst, Int. J. Inorg. Chem. 2012 (2012) 1–9. doi:10.1155/2012/608183.

[12] Z. Xue, P. Wang, A. Peng, T. Wang, Architectural Design of Self-Assembled Hollow Superstructures, Adv. Mater. 31 (2019) 1801441. doi:10.1002/adma.201801441.

[13] W. Wichaita, D. Polpanich, P. Tangboriboonrat, Review on Synthesis of Colloidal Hollow Particles and Their Applications, Ind. Eng. Chem. Res. 58 (2019) 20880–20901. doi:10.1021/acs.iecr.9b02330.

[14] N. Thiwakornkitkul, T. Suteewong, Effect of Morphology of Titanium Dioxide Nanoparticles on Photocatalytic Activity, IOP Conf. Ser. Mater. Sci. Eng. 639 (2019) 012021. doi:10.1088/1757-899X/639/1/012021.

[15] X. Zhang, W. Wang, W. Shen, G. Zhao, J. Wang, Fabrication of hollow cubic silica nanoframes with a fibrous morphology, Mater. Lett. 252 (2019) 31–34. doi:10.1016/j.matlet.2019.05.039.

[16] M.M. Ferrer, A.F. Gouveia, L. Gracia, E. Longo, J. Andrés, A 3D platform for the morphology modulation of materials: first principles calculations on the thermodynamic stability and surface structure of metal oxides: Co_3O_4 , α-Fe_2O_3 , and

In_2O_3, Model. Simul. Mater. Sci. Eng. 24 (2016) 025007. doi:10.1088/0965-0393/24/2/025007.

[17] M.F. Silva, L.A.S. de Oliveira, M.A. Ciciliati, L.T. Silva, B.S. Pereira, A.A.W. Hechenleitner, D.M.F. Oliveira, K.R. Pirota, F.F. Ivashita, A. Paesano, J. Martin Pastor, J. Iñaki Pérez-Landazábal, E.A.G. Pineda, Nanometric particle size and phase controlled synthesis and characterization of γ-Fe_2O_3 or (α + γ)-Fe_2O_3 by a modified sol-gel method, J. Appl. Phys. 114 (2013) 104311. doi:10.1063/1.4821253.

[18] G. Byzynski, C. Ribeiro, E. Longo, Blue to Yellow Photoluminescence Emission and Photocatalytic Activity of Nitrogen Doping in TiO_2 Powders, Int. J. Photoenergy. 2015 (2015) 1–12. doi:10.1155/2015/831930.

[19] M.-C. Tsai, J.-Y. Lee, P.-C. Chen, Y.-W. Chang, Y.-C. Chang, M.-H. Yang, H.-T. Chiu, I.-N. Lin, R.-K. Lee, C.-Y. Lee, Effects of size and shell thickness of TiO2 hierarchical hollow spheres on photocatalytic behavior: An experimental and theoretical study, Appl. Catal. B Environ. 147 (2014) 499–507. doi:10.1016/j.apcatb.2013.09.033.

[20] Y. Zheng, J. Cai, K. Lv, J. Sun, H. Ye, M. Li, Hydrogen peroxide assisted rapid synthesis of TiO2 hollow microspheres with enhanced photocatalytic activity, Appl. Catal. B Environ. 147 (2014) 789–795. doi:10.1016/j.apcatb.2013.10.011.

[21] E.L. da Silva, J.A. Varela, D.K. de Araújo, D.P. Volanti, Microwave aided device for hydrothermal synthesis of nanostructured oxides, particularly obtaining particles of metal oxides, comprises container, in which hydrothermal reaction takes place, and lid for container, BR200815393-A2, 2010.

[22] M. Mohammadikish, Hydrothermal synthesis, characterization and optical properties of ellipsoid shape α-Fe2O3 nanocrystals, Ceram. Int. 40 (2014) 1351–1358. doi:10.1016/j.ceramint.2013.07.016.

[23] J.Q. Qi, J. Lu, Y.W. Sui, Y.Z. He, F.X. Wei, Q.K. Meng, TiO2/Fe2O3 composite obtained through oxidation of Ti-15Fe alloy foil for high-performance supercapacitor electrode, 2016. doi:10.1016/j.matlet.2016.08.002.

[24] E. Madej, N. Spiridis, R.P. Socha, B. Wolanin, J. Korecki, The nucleation, growth and thermal stability of iron clusters on a TiO 2 (110) surface, Appl. Surf. Sci. 416 (2017) 144–151. doi:10.1016/j.apsusc.2017.04.114.

[25] R. Li, Y. Jia, N. Bu, J. Wu, Q. Zhen, Photocatalytic degradation of methyl blue using Fe 2 O 3 /TiO 2 composite ceramics, J. Alloys Compd. 643 (2015) 88–93. doi:10.1016/j.jallcom.2015.03.266.

[26] D. Barreca, G. Carraro, A. Gasparotto, C. Maccato, M.E.A. Warwick, K. Kaunisto, C. Sada, S. Turner, Y. Gönüllü, T.-P. Ruoko, L. Borgese, E. Bontempi, G. Van Tendeloo, H. Lemmetyinen, S. Mathur, Fe 2 O 3 -TiO 2 Nano-heterostructure Photoanodes for Highly Efficient Solar Water Oxidation, Adv. Mater. Interfaces. 2 (2015) 1500313. doi:10.1002/admi.201500313.

[27] Y. Chen, W. Li, J. Wang, Y. Gan, L. Liu, M. Ju, Microwave-assisted ionic liquid synthesis of Ti3+ self-doped TiO2 hollow nanocrystals with enhanced visible-light photoactivity, Appl. Catal. B Environ. 191 (2016) 94–105. doi:10.1016/j.apcatb.2016.03.021.

[28] W. Thongsuwan, P. Singjai, Influence of TiO2/Fe2O3 interfacial layers on optical properties under visible light, Surf. Coatings Technol. 306 (2016) 49–53. doi:10.1016/j.surfcoat.2016.04.026.

[29] J.-C. Wang, J. Ren, H.-C. Yao, L. Zhang, J.-S. Wang, S.-Q. Zang, L.-F. Han, Z.-J. Li, Synergistic photocatalysis of Cr(VI) reduction and 4-Chlorophenol degradation over hydroxylated α-Fe2O3 under visible light irradiation, J. Hazard. Mater. 311 (2016) 11–19. doi:10.1016/j.jhazmat.2016.02.055.

[30] L. Bu, Z. Shi, S. Zhou, Modeling of Fe(II)-activated persulfate oxidation using atrazine as a target contaminant, Sep. Purif. Technol. 169 (2016) 59–65. doi:10.1016/j.seppur.2016.05.037.

[31] G.B. Soares, B. Bravin, C.M.P. Vaz, C. Ribeiro, Facile synthesis of N-doped TiO2 nanoparticles by a modified polymeric precursor method and its photocatalytic properties, Appl. Catal. B Environ. 106 (2011) 287–294. doi:10.1016/j.apcatb.2011.05.018.

[32] K. Wu, Y. Xie, J. Zhao, H. Hidaka, Photo-Fenton degradation of a dye under visible light irradiation, J. Mol. Catal. A Chem. 144 (1999) 77–84. doi:10.1016/S1381-1169(98)00354-9.

[33] A. Banisharif, A.A. Khodadadi, Y. Mortazavi, A. Anaraki Firooz, J. Beheshtian, S. Agah, S. Menbari, Highly active Fe2O3-doped TiO2 photocatalyst for degradation of trichloroethylene in air under UV and visible light irradiation: Experimental and computational studies, Appl. Catal. B Environ. 165 (2015) 209–221. doi:10.1016/j.apcatb.2014.10.023.

[34] Y.Y. Mi, S.J. Wang, J.W. Chai, J.S. Pan, C.H.A. Huan, Y.P. Feng, C.K. Ong, Effect of nitrogen doping on optical properties and electronic structures of SrTiO3 films, Appl. Phys. Lett. 89 (2006) 231922. doi:10.1063/1.2403181.

[35] K. Gopinath, S. Kumaraguru, K. Bhakyaraj, S. Thirumal, A. Arumugam, Eco-friendly synthesis of TiO2, Au and Pt doped TiO2 nanoparticles for dye sensitized solar cell applications and evaluation of toxicity, Superlattices Microstruct. 92 (2016) 100–110. doi:10.1016/j.spmi.2016.02.012.

[36] M. Asiltürk, F. Sayılkan, E. Arpaç, Effect of Fe3+ ion doping to TiO2 on the photocatalytic degradation of Malachite Green dye under UV and vis-irradiation, J. Photochem. Photobiol. A Chem. 203 (2009) 64–71. doi:10.1016/j.jphotochem.2008.12.021.

[37] A. V. Vinogradov, V. V. Vinogradov, A. V. Agafonov, A simple preparation of highly photoactive Fe(III)-doped titania nanocrystals by annealing-free approach, J. Alloys Compd. 581 (2013) 675–678. doi:10.1016/j.jallcom.2013.07.192.

[38] S. Liu, J. Zhu, X. Guo, J. Ge, H. Wu, Preparation of ??-Fe2O3-TiO2/fly ash cenospheres photocatalyst and its mechanism of photocatalytic degradation, Colloids Surfaces A Physicochem. Eng. Asp. 484 (2015) 434–440. doi:10.1016/j.colsurfa.2015.08.033.

[39] L. Kong, C. Wang, F. Wan, H. Zheng, X. Zhang, Synergistic effect of surface self-doping and Fe species-grafting for enhanced photocatalytic activity of TiO2 under visible-light, Appl. Surf. Sci. 396 (2017) 26–35. doi:10.1016/j.apsusc.2016.11.051.